

Evaluation of sinus/edge corrected ZTE-based attenuation correction in brain PET/MRI

Jaewon Yang, PhD¹, Florian Wiesinger², Sandeep Kaushik³, Dattesh Shanbhag³, Thomas A. Hope, MD¹, Peder E. Z. Larson¹, and Youngho Seo, PhD¹

¹Department of Radiology and Biomedical Imaging, University of California, San Francisco, San Francisco, CA

²GE Global Research, Munich, Germany

³GE Global Research, Bangalore, India

Corresponding author: Jaewon Yang, PhD

Associate Specialist of Radiology and Biomedical Imaging, UCSF

185 Berry Street, Suite 350, San Francisco, CA 94107

Tel: 415/353-4910

Fax: 415/353-9423

Short running title: sinus/edge corrected ZTAC

Word count: 4899

Financial support: This project was supported in part by grant from GE Healthcare.

ABSTRACT

Purpose: In brain positron emission tomography/magnetic resonance imaging (PET/MRI), the major challenge of zero-echo-time (ZTE)-based attenuation correction (ZTAC) is the misclassification of air/tissue/bone mixtures or their boundaries. Our study aimed to evaluate a sinus/edge corrected (SEC) ZTAC ($ZTAC_{SEC}$), relative to an “uncorrected (UC)” ZTAC ($ZTAC_{UC}$) and a computed tomography (CT) atlas-based attenuation correction (ATAC).

Materials and Methods: Whole-body fluorodeoxyglucose PET/MRI scans were performed for twelve patients, following PET/CT scans. Only data acquired at a bed station that includes the head were employed for this study. Using PET data from PET/MRI, $ZTAC_{UC}$, $ZTAC_{SEC}$, ATAC and reference CT-based attenuation correction (CTAC) were applied to PET attenuation correction. For $ZTAC_{UC}$, the bias-corrected and normalized ZTE was converted to pseudoCT with air (-1000 HU for $ZTE < 0.2$), soft-tissue (42 HU for $ZTE > 0.75$), and bone ($-2000*(ZTE-1) + 42$ HU for $0.2 \leq ZTE \leq 0.75$). Afterwards, in the pseudoCT, sinus/edges were automatically estimated as a binary mask through morphological processing and edge detection. In the binary mask, the overestimated values were rescaled below 42 HU for $ZTAC_{SEC}$. For ATAC, the atlas deformed to MR in-phase was segmented to air, inner-air, soft-tissue, and continuous bone. For the quantitative evaluation, PET mean uptake values were measured in twenty 1 ml volumes-of-interest distributed throughout brain tissues. The PET uptakes were compared using a paired *t*-test. An error histogram was employed to show the distribution of voxel-based PET uptake differences.

Results: Compared to CTAC, $ZTAC_{SEC}$ achieved the overall PET quantification accuracy ($0.2 \pm 2.4\%$, $p = 0.23$) similar to CTAC, in comparison with $ZTAC_{UC}$ ($5.6 \pm 3.5\%$, $p < 0.01$) and ATAC ($-0.9 \pm 5.0\%$, $p = 0.03$). Specifically, a substantial improvement with $ZTAC_{SEC}$ ($0.6 \pm 2.7\%$, $p < 0.01$) was found in cerebellum region, in comparison with $ZTAC_{UC}$ ($8.1 \pm 3.5\%$, $p < 0.01$) and ATAC ($-4.1 \pm 4.3\%$, $p < 0.01$). The histogram of voxel-based uptake differences demonstrated that $ZTAC_{SEC}$ reduced the magnitude and variation of errors substantially, compared to $ZTAC_{UC}$ and ATAC.

Conclusion: Sinus/edge corrected ZTAC can provide an accurate PET quantification in brain PET/MRI, comparable to the accuracy achieved by CTAC, particularly in the cerebellum.

INTRODUCTION

Development of positron emission tomography combined with magnetic resonance imaging (PET/MRI) devices has evolved in recent years, and time-of-flight (TOF) capability has been added to PET/MRI (1). Using PET/MRI, previous studies have demonstrated its potential for neurological imaging in order to investigate brain function, tumor, and degenerative diseases (2). However, since there is no direct way to derive photon attenuation coefficients from MRI for PET attenuation correction (AC), there have been substantial concerns about PET quantification accuracy with regards to MR-based attenuation correction (MRAC) (3).

MRAC methods are categorized into segmentation-based, atlas-based, and PET emission-based approaches (4). Segmentation-based methods derive AC maps by classifying Dixon-based MR images into tissue classes (e.g., air, lung, fat, and soft tissue) to which uniform (i.e., single value) linear attenuation coefficients are assigned (5). The Dixon-based segmentation disregards bone anatomy due to low proton density and short-lived signals (6), even though PET signals are substantially attenuated in bone structures (7). Atlas-based methods include bone structures into AC maps using a single computed tomography (CT) atlas (8), multiple CT atlases (9) or a pair of MR model and skull mask (10) through registration. Despite no physical relationship between MRI and CT, advanced atlas-based methods have proposed a statistical model to convert MR intensities to CT numbers using machine learning methods (i.e., training pairs of matched MR/CT images) (11). Without depending on MRI or atlas images, PET emission-based methods have also demonstrated clinical feasibility for simultaneous estimation of attenuation and activity maps using TOF emission data (12).

Zero-echo-time (ZTE) MRI has demonstrated a possibility to overcome the drawbacks of missing bone signals (i.e., limitation of Dixon-based segmentation), capturing rapidly decaying bone signals (13). Similarly, ultrashort-echo-time (UTE) MRI also can capture bone signals, with greater flexibility in image contrast and field of views (FOV) but with increased acoustic noise and greater sensitivity to gradient fidelity compared to ZTE (14). UTE is typically used to derive MRAC based on $T2^*$ relaxation differences (15). The disadvantage of such $T2^*$ -based approaches is that they are sensitive to short- $T2^*$ values resulting from off-resonance, particularly in regions of large magnetic susceptibility differences such as the sinuses, and other short- $T2^*$ tissues such as tendons, all of which may be misclassified as bone. Meanwhile, ZTE-based MRAC methods

have utilized proton-density differences to contrast bone against soft tissues and air (13) and are more robust to off-resonance effects than T2*-based methods.

A preliminary ZTE-based attenuation correction (ZTAC) method was evaluated for brain PET AC in a TOF PET/MRI system (SIGNA PETMR, GE Healthcare) (16). The preliminary ZTAC demonstrated more accurate AC in comparison with the atlas-based attenuation correction (ATAC) protocol in the scanner; but the major challenge of ZTAC was the misclassification of air/tissue/bone mixtures (e.g., sinus or mastoid) or their edges (e.g., skin or trachea) as bone, resulting in overestimated PET quantification. Inaccurate ATAC in the cerebellum is also a well-known problem because the level of sinuses, where air, soft tissue, and bone structures are mixed, is a challenge for accurate registration (3). Therefore, it is important to improve the accuracy of ZTAC near the skull base for neurological PET/MRI studies because target-to-reference ratio, a widely used quantification technique, uses cerebellum as a reference for PET quantification (17). Our study aimed to evaluate a sinus/edge corrected (SEC) ZTE-based attenuation correction (ZTAC_{SEC}), relative to an “uncorrected (UC)” ZTAC (ZTAC_{UC}) and the ATAC.

MATERIALS AND METHODS

Patient information

The patient study was approved by the Institutional Review Board and all patients signed an informed consent before the examinations. Twelve patients (5 men and 7 women) had whole-body fluorodeoxyglucose (FDG) PET/CT for clinical indications, immediately followed by whole-body PET/MRI. There was no second administration of FDG for PET/MRI. The average patient age was 60.8 ± 9.5 y (44–74 y); The average weight was 71.9 ± 13.5 kg (54.4–97.5 kg); The average administered dose of FDG was 297.9 ± 58.9 MBq (218.3–392.2 MBq). For PET/MRI, the average scan duration of the whole brain was 245.0 ± 92.5 s (135–390 s), and the average time difference between injection and scan was 147.1 ± 23.7 min (119.6–188.6 min). No pathology in the brain was reported. Only PET/MRI/CT data acquired at a bed station that includes the head were employed for this study.

PET/CT

PET/CT examinations were performed on Discovery PET/CT (GE Healthcare, Waukesha, WI) or Biograph HiRez 16 (Siemens Healthcare, Germany). The helical CT scans (120 kVp; 105-599 mA; rotation time: 0.5 s; pitch: 0.98 and 0.75; 39.37 and 34.45 mm/rotation for GE and Siemens systems, respectively) were performed for PET AC. CT images were reconstructed with an axial FOV of 700 and 500 mm, a slice thickness of 3.75 and 5.00 mm, a matrix size of 512×512, voxel sizes of 2.73×2.73×3.75 and 1.95×1.95×5.00 mm³ for GE and Siemens systems, respectively. For the head station, the FOV of 500 mm was enough to cover the whole head for all PET data acquired in PET/MRI.

PET/MRI

TOF-PET/MRI acquisition was performed on a SIGNA PET/MR (GE Healthcare, Waukesha, WI). PET had 600 mm transaxial FOV and 250 mm axial FOV, with TOF timing resolution of approximately 400 ps and average measured sensitivity of 22.65 cps/kBq (18). While PET data were acquired, 3D spoiled gradient echo T1-weighted images (repetition time (TR) ~ 4 ms, 1st echo time/2nd echo time (TE₁/TE₂) = 1.3/2.6 ms, flip angle: 5 degrees, acquisition time: 18 sec) were acquired for PET AC, using the head and neck coil array. This sequence generated in-phase, out-of-phase, fat and water images using the Dixon method (transaxial FOV: 500 mm, slice spacing: 2.6 mm, matrix size: 256×256×120, and voxel size: 1.95×1.95×5.2 mm³). Additionally, proton density-weighted ZTE images (transaxial FOV: 262 or 490 mm, matrix size: 110×110×110 or 192×192×192, voxel size: 2.4×2.4×2.4 mm³ or 2.6×2.6×2.6 mm³) were acquired using the same head and neck coil array with two sequences (TR ~ 0.7 ms, TE: 0 ms, flip angle: 0.6 degree, transmit/receive switching delay: ~28 μs, readout duration: 440 or 384 μs, acquisition time: 41 or 84 s). These were 3D radial acquisitions without slab selection, so there was no preferential scan direction. The FOV was isotropic as well as the spatial resolution. The center of k-space was filled in by acquiring an additional set of low-frequency projections with lower gradient strengths (19). The smaller FOV ZTE image was acquired for dedicated brain imaging (n=8), and the larger FOV ZTE image was acquired as a part of the whole-body imaging (n=4). The contrast was equivalent between the two sequences: they used the same TE, TR, and flip angles. The other key consideration

when imaging bone with MRI is signal decay during the readout (20), and both sequences had nearly identical readout durations to yield nearly identical relative bone signal. These ZTE-sequences were implemented and tested as potential commercial products.

Uncorrected ZTAC (ZTAC_{UC})

Before sinus/edge correction was applied, ZTE images were converted to pseudoCT as follows: First, ZTE values were bias-corrected (21) and normalized by the median tissue value. Then, ZTE values were converted to CT numbers (Hounsfield Unit: HU) by applying simple thresholds for air (-1000 HU for ZTE < 0.2) and soft-tissue (42 HU for ZTE > 0.75) and linear transformation for bone ($-2000 \times (ZTE - 1) + 42$ HU for intermediate ZTE values) (Fig. 1). In ZTAC_{UC}-derived pseudoCT, air/tissue interfaces (e.g. skin and trachea), air/tissue mixtures (e.g., sinus), air/bone mixtures (e.g., mastoid) are typically misclassified. This was because these mixtures result in ZTE signal intensities that are in between air and soft tissue, just like bone. For example, as shown in Fig. 1, air/tissue mixtures in the sinus were partially misclassified as bone. This ZTAC_{UC}-derived pseudoCT was a prior for ZTAC_{SEC}-derived pseudoCT.

Sinus/edge corrected ZTAC (ZTAC_{SEC})

To reduce the effect of the misclassification above, sinus/edge correction was applied to ZTAC_{UC}-derived pseudoCT where a binary mask including the sinus and air/tissue interfaces (edges) was estimated. The overestimated CT values in the binary mask were rescaled by the following formula in order to make them at least smaller than 42 HU (soft tissue):

$$\text{CT (HU) in the binary mask} = \min ((1042 \times \text{ZTE}) / 0.75 - 1000, 42)$$

The binary mask was generated as follows: First, the “peak” of the sinus was defined as the axial slice with the most internal air distribution, as measured on ZTE and shown by the red line in the “Sinus peak” in Fig. 1.

Second, a square box (3.5cm above to 0.5cm below the peak, covering a width of ± 2.5 cm) was defined for the nasal area, in which the sinus was segmented and refined by morphological processing (Fig. 1, Sinus mask).

Third, air/tissue edges were estimated and refined by edge detection and morphological processing (Fig. 1, Edge

mask). Finally, the sinus mask and the edge mask were combined into a whole-brain binary mask. Note that ZTAC_{SEC} was implemented and tested as a potential commercial product.

ATAC

The atlas-based pseudoCT is the current implementation for brain PET AC in a SIGNA PET/MR. PseudoCT using an atlas was prepared by segmenting the atlas (AT) into four tissue classes with air (-1000 HU for outside of head), sinus (-800 HU for AT < -200 HU), soft-tissue (42 HU for intermediate AT), and bone (consistent HU for AT > 300 HU with erosion). Before tissue classification, the single representative atlas was registered to patient MR (in-phase) images by contour-based rigid and nonrigid registration (8).

CTAC

Reference CT from PET/CT was prepared by removing its background (e.g., table) and registering to ZTE using Advanced Normalization Tools (22).

The three kinds of MRAC (ZTAC_{UC}, ZTAC_{SEC}, and ATAC) pseudoCTs and reference CT were converted to AC maps through bi-linear transform (23), based on the CT energy of 120 kVp for both pseudoCT and CT. Attenuation template of nonpatient components such as a table and head coil were developed by the vendor and added appropriately to the image space. The resulting PET volumes were named PET/ZTAC_{UC}, PET/ZTAC_{SEC}, PET/ATAC, and PET/CTAC, corresponding to the AC methods above, respectively.

PET reconstruction

PET images were reconstructed using TOF Ordered Subsets Expectation Maximization because it has demonstrated reduced errors caused by inaccurate MRAC (24) (point spread function kernel derived from the PET detector response, 4 iterations, 28 subsets, a matrix size of 256×256 over 256 mm transaxial FOV, a voxel size of 1.0×1.0×2.78 mm³, with a 3.0 mm full-width at half-maximum (FWHM) in-plane Gaussian filter followed by axial filtering with a 3-slice 1:4:1 kernel). The detector point spread function, also known known as

the detector response function, was employed to reduce detector blurring for resolution recovery (25). The filtering was a standard procedure recommended by the vendor for reducing high frequency noise in PET images. The PET reconstruction with all implemented corrections (i.e., random, scatter, and normalization) was performed using an offline reconstruction toolbox (REL_1_26, GE Healthcare, Waukesha, WI) in MATLAB (MathWorks, Natick, MA).

Data analysis

Twenty volumes-of-interest (VOIs, $10 \times 10 \times 3$ voxels = $10 \times 10 \times 8.34$ mm³ \approx 1 ml) were placed close to cortical bone and higher uptake regions in PET images at the left and right side of thalamus, corpus callosum, temporal lobe, frontal lobe, occipital lobe, cerebral cortex, and cerebellum (Fig. 2). Specifically, four pairs of VOIs (anterior, posterior, center, and inferior) were localized in the cerebellum, considering its sensitivity to the accuracy of sinus segmentation (3). For each patient dataset, the VOIs were manually placed in similar positions throughout brain tissues, in order to preserve the original quality of patient-specific PET images for reliable patient-specific analysis. Using PET/CTAC (PET reconstruction using CTAC) as a basis of comparison, PET uptake differences (kBq/ml) between PET/CTAC and PET/MRAC (PET uptake values with ZTAC_{UC}, ZTAC_{SEC}, or ATAC) were calculated for each VOI as follows:

$$\text{Diff (kBq/ml)} = \text{mean}(\text{voxels of VOI}_{\text{MRAC}}) - \text{mean}(\text{voxels of VOI}_{\text{CTAC}})$$

$$\text{Diff (\%)} = [\text{mean}(\text{voxels of VOI}_{\text{MRAC}}) - \text{mean}(\text{voxels of VOI}_{\text{CTAC}})] / \text{mean}(\text{voxels of VOI}_{\text{CTAC}}) * 100$$

Patient-specific and VOI-specific results were presented across 12 patients and corresponding 20 VOIs through box plots that can show statistical distribution of PET uptake differences. A paired *t*-test was performed for comparing the PET uptake differences of PET/MRAC from reference PET/CTAC. A *p*-value < 0.05 was considered to indicate statistical significance.

A histogram was employed to show the distribution of voxel-based PET uptake differences (PET/CTAC – PET/MRAC) within the standardized uptake value (SUV: image-derived uptake (MBq/ml)/injection dose (MBq) × patient's weight (g)) range of 0.5-15.0 (g/ml) across all subjects. Additionally, pseudoCT, AC maps, and PET images of representative patients were illustrated according to the AC methods, specifically focusing

on the cerebellum and mastoid.

RESULTS

The mean uptake difference (\pm standard deviation [SD]) of PET/ZTAC_{SEC} from PET/CTAC was $0.2\pm 2.4\%$ ($p = 0.23$); while, the difference of PET/ZTAC_{UC} was $5.6\pm 3.5\%$ ($p < 0.01$) and the difference of PET/ATAC was $-0.9\pm 5.0\%$ ($p = 0.03$) (Table 1). All *t*-tests were statistically significant except the *t*-test between PET/ZTAC_{SEC} and PET/CTAC, implying PET/ZTAC_{SEC} was statistically similar with PET/CTAC. In the Bland-Altman plot (Fig. 3), most of the circles with ZTAC_{UC} were positioned in positive areas, indicating substantial overestimation of PET uptake in comparison with CTAC; while, most of the triangles with ATAC were more scattered over negative areas (SD: 5.0%) than the circles with ZTAC_{UC} (SD: 3.5%). On the contrary, the stars with ZTAC_{SEC} were positioned within the range of $\pm 5\%$ with the smallest variation (SD: 2.5%).

However, the results were patient and VOI-location dependent. In Fig. 4A, the improved *inter*- and *intra*-patient variations by ZTAC_{SEC} was consistent with the overall result as above. In terms of *inter*-patient variation, PET uptake differences with ZTAC_{SEC} in the boxes (i.e., 25th – 75th percentiles) of all patients stayed within the boundaries of $\pm 5\%$. Also, in terms of *intra*-patient variation, the 25th – 75th percentiles with ZTAC_{SEC} usually had a smaller or comparable range compared to those with ZTAC_{UC} and ATAC. In Fig. 4B, the reduction of VOI-dependent variations by ZTAC_{SEC} was also consistent with the overall result as above: PET uptake differences with ZTAC_{SEC} in the boxes of all VOIs stayed within the boundaries of $\pm 5\%$. Specifically, ZTAC_{SEC} improved PET quantification accuracy ($0.6\pm 2.7\%$, range: $-6.6 - 8.1\%$, $p < 0.01$) significantly in the cerebellum at the level of sinus, compared to the accuracy of ZTAC_{UC} ($8.1\pm 3.5\%$, range: $1.3 - 19.0\%$, $p < 0.01$) and that of ATAC ($-4.1\pm 4.3\%$, range: $-15.0 - 4.6\%$, $p < 0.01$).

The histogram of voxel-based PET uptake differences (PET/MRAC – PET/CTAC) across all patients demonstrated that ZTAC_{SEC} reduced the magnitude and variation of errors substantially, compared to those of ZTAC_{UC} and ATAC (Fig. 5). The 25 and 75 percentiles (vertical yellow lines) demonstrated that the uptake differences of PET/ZTAC_{SEC} and PET/ATAC were symmetrically distributed from the origin (zero error), though those of PET/ZTAC_{UC} were mostly distributed in the positive (overestimated) error zone.

The voxel-based comparison was consistent with the patient-dependent comparison (Fig, 6). In Fig. 6A (patient 5, sagittal view), ZTAC_{SEC}-derived pseudoCT (1st row) was more consistent with reference CT at the sinus region (arrows); while, ZTAC_{UC}-derived pseudoCT illustrates misclassified bone signals and ATAC-derived pseudoCT illustrates geometrical offsets from reference CT at anatomical structures such as sinus, skull, etc. Consistently, ZTAC_{SEC}-derived AC maps (2nd row) illustrates the improved sinus, compared to ZTAC_{UC}- and ATAC-derived AC maps. As a result, ZTAC_{SEC} improved PET quantification in the cerebellum (3rd row, arrows) at the level of sinus without substantial over/under-estimation; while, PET/ZTAC_{UC} was consistently overestimated throughout the brain but more substantially at the level of sinus and PET/ATAC was overestimated at skull top but underestimated at the skull base. However, in Fig. 6B (patient 5, coronal view), misclassified bone signals at the mastoid were not fixed in ZTAC_{SEC}-derived pseudoCT (1st row) because the binary mask did not include the mastoid region for correction (Fig. 1). The impact of the mastoid misclassification in ZTAC_{SEC} was illustrated as slightly overestimated PET uptakes near the mastoid; while, the impact of the mastoid misclassification was negligible in the cerebellum. In Fig. 6C and 6D (patient 8), the similar observations were visually accounted for and specifically in the cerebellum at the level of sinus.

DISCUSSION

The ZTAC_{SEC} was implemented for a potential commercial translation, overcoming the major challenge of ZTAC by correcting misclassified bone signals due to air/tissue/bone mixtures or interfaces. Our results demonstrated that ZTAC_{SEC} (mean uptake difference: $0.2 \pm 2.4\%$) outperformed ZTAC_{UC} ($5.6 \pm 3.5\%$) and ATAC ($-0.9 \pm 5.0\%$) for PET quantification accuracy and precision, compared to CTAC. Specifically, a significant improvement with ZTAC_{SEC} was found in the cerebellum region at the level of sinus, the most vulnerable area affected by inaccurate MRAC (3,16).

Inter-patient anatomical and bone-density variability played a key role in the performance of each method (24). The ATAC method relied on a single atlas CT, which could not capture the range of inter-patient variability in our subjects. This caused the error variation of PET/ATAC (SD: 5.0%) to be larger than those of PET/ZTAC_{SEC} (SD: 2.4%) and PET/ZTAC_{UC} (SD: 3.5%). ZTAC reduced the variation by removing the need of

registration and by estimating bone density through a linear conversion of ZTE bone to CT values. The remaining patient-specific error variation of PET/ZTAC_{SEC} (2.4%) was largely because sinus/edge correction could not consistently capture patient-specific mixtures of air/tissue/bone in the sinuses. In terms of the inter-regional variability, the variability was the most severe in the cerebellum at the level of sinuses for both PET/ATAC and PET/ZTAC_{UC}. As air, soft tissue, and bone structures are mixed in the sinuses, it was a challenge to achieve accurate registration for ATAC (Fig. 6) and to classify the mixed signals accurately for ZTAC_{UC}.

In a prior study using a preliminary ZTAC method (16), similar to the ZTAC_{UC}, the overall error ($-0.1 \pm 2.3\%$) was smaller than the error of ZTAC_{UC} ($5.6 \pm 3.5\%$). The larger error of ZTAC_{UC} could be derived from the following differences as our ZTE-CT conversion was optimized for ZTAC_{SEC}-derived pseudoCT: the segmentation thresholds for bone class (our ZTACs vs. preliminary ZTAC: $0.2 < ZTE < 0.75$ vs. $0.25 < ZTE < 0.85$) and the slope of linear correlation between ZTE and CT values (our ZTACs vs. preliminary ZTAC: 2000 vs. 2400). The overall error of ZTAC_{SEC} in our study ($0.2 \pm 2.4\%$ error) was comparable to that of the preliminary ZTAC study. However, for the cerebellum, which was the most vulnerable to AC errors in the sinus, the average error of ZTAC_{SEC} ($0.6 \pm 2.7\%$) was much lower than that of the preliminary ZTAC study ($3.31 \pm 1.70\%$) (23).

There were several limitations of our study: One limitation was the small number of patients ($n = 12$). Also, the PET data acquisition was not optimized for dedicated brain PET scans that are typically performed with a longer acquisition time. However, we employed brain PET reconstruction with a small FOV reconstruction (256 mm in the transaxial view) and a high number of iterations, resulting in a smaller voxel size ($1.0 \times 1.0 \times 2.78 \text{ mm}^3$) for brain PET quality assurance. Although both the small voxel size and shorter scan time might cause a low signal-to-noise ratio, this problem was mitigated in the VOI-based analysis by averaging the values of $10 \times 10 \times 3$ (300) voxels located in higher activity regions. Also, two different ZTE MRI protocols were used, but the differences between these protocols are likely negligible for ZTAC processing: They were designed to provide nearly identical bone to soft tissue contrast, the key parameter in the pseudoCT generation method, and provided similar voxel sizes. We expect the impact of resolution differences on MRAC accuracy to

be small, considering that AC maps were substantially blurred due to Gaussian post-filtering with 10 mm full-width at half-maximum (this AC map filtering was a standard procedure recommended by the vendor). We observed no consistent differences in the AC maps between the protocols. Another limitation was that two different CT scanners might cause an impact on the quality of reference CT in the course of registration. Considering the low resolution of AC maps ($4.69 \times 4.69 \text{ mm}^2$), however, the potential impact of CT quality variation was likely suppressed through Gaussian post-filtering with 10 mm full-width at half-maximum at the final step of AC map generation. Additionally, the manual localization of VOIs might cause operator-dependent results. To mitigate potential errors, a single operator performed all localization. Compared to using a brain template, using VOIs with small sizes ($\approx 1 \text{ ml}$) and higher uptake preserved the sensitivity of localized errors with regards to the bone and sinus, and reduced potential bias of errors amplified by relatively lower uptake regions (24). Finally, the current correction algorithm did not estimate the mastoid with air/bone mixtures, as illustrated in Fig. 1, resulting in slight overestimation of PET uptakes near the mastoid. If mastoid regions could be estimated accurately, the accuracy of $ZTAC_{SEC}$ would be more improved near the mastoid region.

CONCLUSION

We evaluated the newly implemented, sinus/edge corrected $ZTAC$ for a potential commercial product. Our results demonstrated that $ZTAC_{SEC}$ improved PET quantification accuracy over $ZTAC_{CUC}$ and $ATAC$, particularly in the cerebellum at the level of sinus.

ACKNOWLEDGMENTS

The authors would like to thank Michel Tohme, PhD, Mehdi Khalighi, PhD, and Floris Jansen, PhD of GE Healthcare for the support of the offline PET/MR reconstruction toolkit. The authors also thank Vahid Ravanfar, BS, for his support to perform PET/MRI scans. This project was supported in part by grant from GE Healthcare.

REFERENCES

1. Iagaru A, Mittra E, Minamimoto R, et al. Simultaneous whole-body time-of-flight 18F-FDG PET/MRI: a pilot study comparing SUVmax with PET/CT and assessment of MR image quality. *Clin Nucl Med*. 2015;40:1-8.
2. Nensa F, Beiderwellen K, Heusch P, Wetter A. Clinical applications of PET/MRI: current status and future perspectives. *Diagn Interv Radiol*. 2014;20:438-447.
3. Visvikis D, Monnier F, Bert J, Hatt M, Fayad H. PET/MR attenuation correction: where have we come from and where are we going? *Eur J Nucl Med Mol Imaging*. 2014;41:1172-1175.
4. Bezrukov I, Mantlik F, Schmidt H, Scholkopf B, Pichler BJ. MR-based PET attenuation correction for PET/MR imaging. *Semin Nucl Med*. 2013;43:45-59.
5. Martinez-Moller A, Souvatzoglou M, Delso G, et al. Tissue classification as a potential approach for attenuation correction in whole-body PET/MRI: evaluation with PET/CT data. *J Nucl Med*. 2009;50:520-526.
6. Du J, Carl M, Bydder M, Takahashi A, Chung CB, Bydder GM. Qualitative and quantitative ultrashort echo time (UTE) imaging of cortical bone. *J Magn Reson*. 2010;207:304-311.
7. Andersen FL, Ladefoged CN, Beyer T, et al. Combined PET/MR imaging in neurology: MR-based attenuation correction implies a strong spatial bias when ignoring bone. *Neuroimage*. 2014;84:206-216.
8. Wollenweber SD, Ambwani S, Delso G, et al. Evaluation of an atlas-based PET head attenuation correction using PET/CT & MR patient data. *IEEE Trans Nucl Sci*. 2013;60:3383-3390.
9. Burgos N, Cardoso MJ, Thielemans K, et al. Attenuation correction synthesis for hybrid PET-MR scanners: application to brain studies. *IEEE Trans Med Imaging*. 2014;33:2332-2341.
10. Koesters T, Friedman KP, Fenchel M, et al. Dixon sequence with superimposed model-based bone compartment provides highly accurate PET/MR attenuation correction of the brain. *J Nucl Med*. 2016;57:918-924.
11. Huynh T, Gao Y, Kang J, et al. Estimating CT image from MRI data using structured random forest and auto-context model. *IEEE T Med Imaging*. 2016;35:174-183.
12. Berker Y, Li Y. Attenuation correction in emission tomography using the emission data--A review. *Med Phys*. 2016;43:807-832.
13. Wiesinger F, Sacolick LI, Menini A, et al. Zero TE MR bone imaging in the head. *Magn Reson Med*. 2016;75:107-114.
14. Larson PEZ, Han MS, Krug R, et al. Ultrashort echo time and zero echo time MRI at 7T. *Magn Reson Mater Phy*. 2016;29:359-370.
15. Ladefoged CN, Benoit D, Law I, et al. Region specific optimization of continuous linear attenuation coefficients based on UTE (RESOLUTE): application to PET/MR brain imaging. *Phys Med Biol*. 2015;60:8047-8065.

16. Sekine T, Ter Voert EE, Warnock G, et al. Clinical evaluation of ZTE attenuation correction for brain FDG-PET/MR imaging-comparison with atlas attenuation correction. *J Nucl Med.* 2016;57:1927-1932.
17. Su Y, Rubin BB, McConathy J, et al. Impact of MR-based attenuation correction on neurologic PET studies. *J Nucl Med.* 2016;57:913-917.
18. Grant AM, Deller TW, Khalighi MM, Maramraju SH, Delso G, Levin CS. NEMA NU 2-2012 performance studies for the SiPM-based ToF-PET component of the GE SIGNA PET/MR system. *Med Phys.* 2016;43:2334.
19. Wu Y, Dai G, Ackerman JL, et al. Water- and fat-suppressed proton projection MRI (WASPI) of rat femur bone. *Magn Reson Med.* 2007;57:554-567.
20. Rahmer J, Bornert P, Groen J, Bos C. Three-dimensional radial ultrashort echo-time imaging with T2 adapted sampling. *Magn Reson Med.* 2006;55:1075-1082.
21. Tustison NJ, Avants BB, Cook PA, et al. N4ITK: improved N3 bias correction. *IEEE Trans Med Imaging.* 2010;29:1310-1320.
22. Avants BB, Tustison N, Song G. Advanced normalization tools (ANTs). *Insight J 2.* 2009:1-35.
23. Lonn AHR. Evaluation of method to minimize the effect of X-ray contrast in PET-CT attenuation correction. *2003 IEEE Nucl Sci Symposium, Conference Record, Vols 1-5.* 2004:2220-2221.
24. Yang J, Jian Y, Jenkins N, et al. Quantitative evaluation of atlas-based attenuation correction for brain PET imaging in an integrated time-of-flight PET/MRI system. *Radiology.* 2017 (In press).
25. Rahmim A, Qi J, Sossi V. Resolution modeling in PET imaging: theory, practice, benefits, and pitfalls. *Med Phys.* 2013;40:064301.

Table 1. PET uptake differences (Diff: mean \pm SD) between reference PET/CTAC and PET/MRAC (uncorrected ZTAC [ZTAC_{UC}], sinus/edge corrected ZTAC [ZTAC_{SEC}], ATAC) across all 240 VOIs. A paired *t*-test was performed for the pair of PET/CTAC and PET/MRAC.

	Diff (kBq/ml)	Diff (%)	<i>p</i> -value
PET/ZTAC _{UC}	0.79 \pm 0.52	5.6 \pm 3.5	<.01
PET/ZTAC _{SEC}	0.03 \pm 0.33	0.2 \pm 2.4	0.23
PET/ATAC	-0.10 \pm 0.71	-0.9 \pm 5.0	0.03

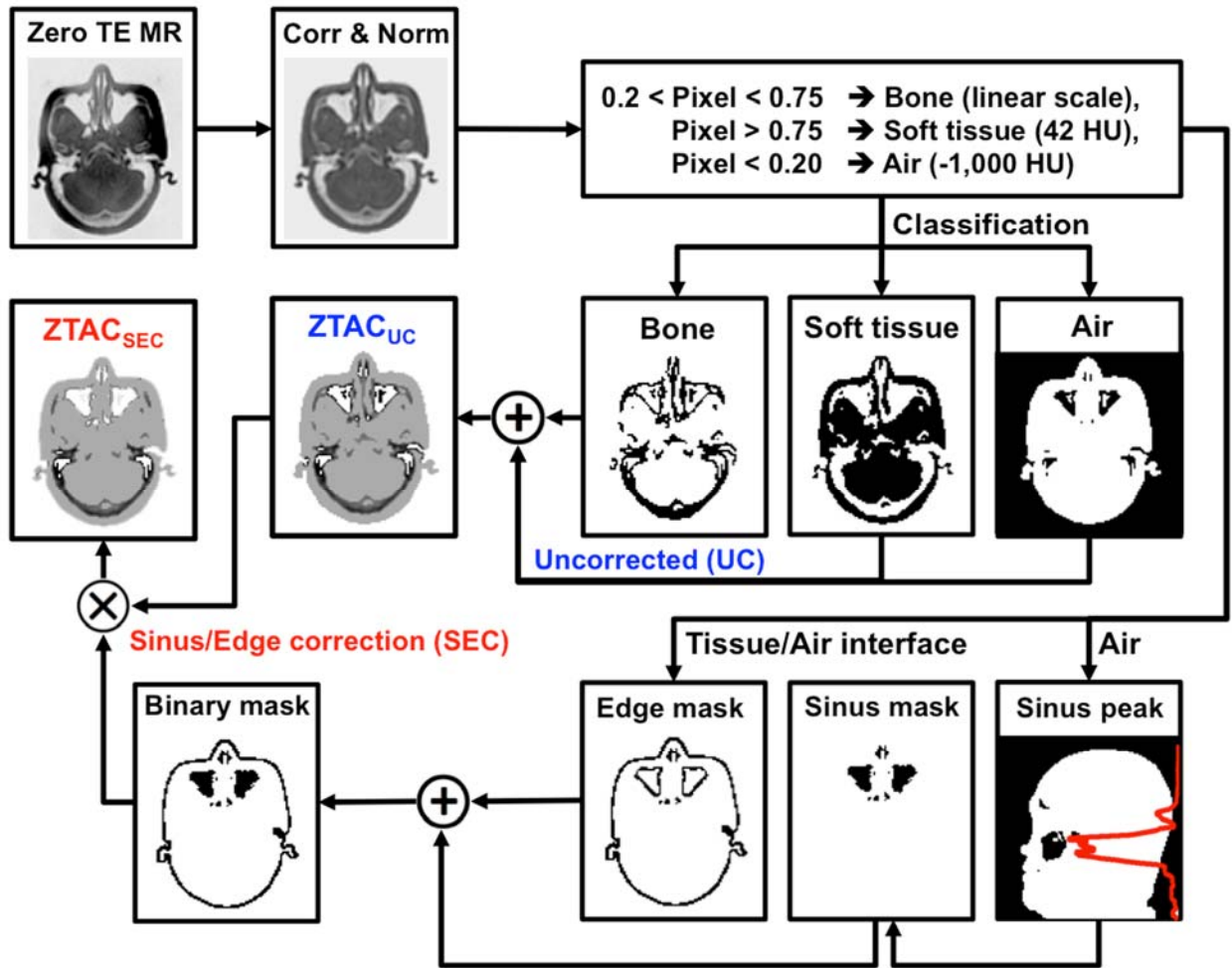


Fig. 1. Workflow of generating pseudoCT from ZTE images: sinus/edge corrected ZTAC (ZTAC_{SEC}) and uncorrected ZTAC (ZTAC_{UC}). In the binary mask, false-positive bone pixels were corrected to stay below 42 HU (soft-tissue).

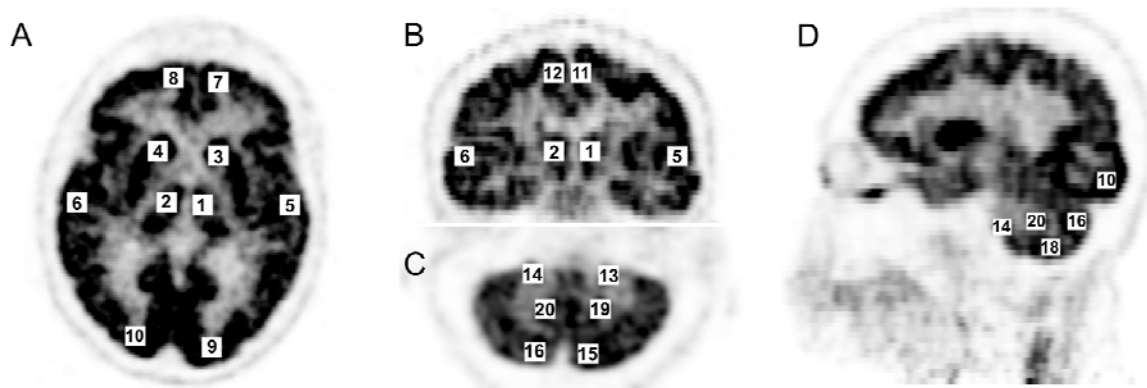


Fig. 2. Localization of twenty volumes of interest (VOIs) for VOI-based quantification: (A) axial brain, (B) coronal brain, (C) axial cerebellum, (D) sagittal brain with sinus and cerebellum: left-right (1-2) thalamus, (3-4) corpus callosum, (5-6) temporal lobe, (7-8) frontal lobe, (9-10) occipital lobe, (11-12) cerebral cortex, (13-20) cerebellum at anterior (13-14), posterior (15-16), inferior (17-18) and center (19-20) positions.

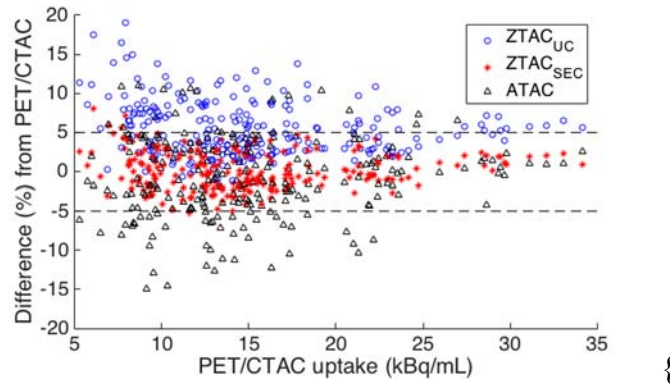
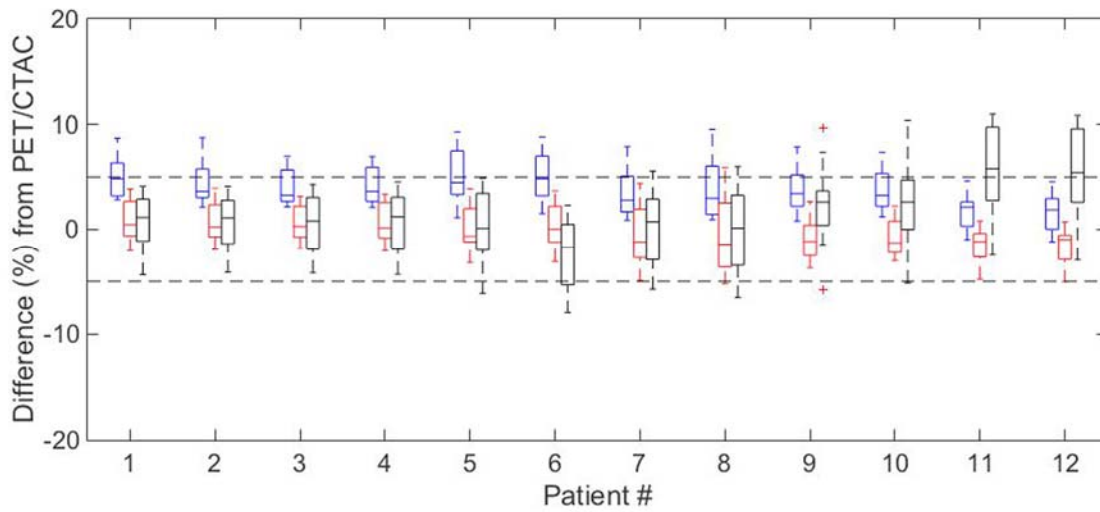


Fig. 3. Bland-Altman plot of 240 VOIs of 12 patients for PET uptake differences (%) with MRAC (ZTAC_{UC}, ZTAC_{SEC}, ATAC) from PET with CTAC (PET/CTAC). PET/ZTAC_{SEC} (red stars) was close to zero mean difference mostly within $\pm 5\%$ boundaries.

A



B

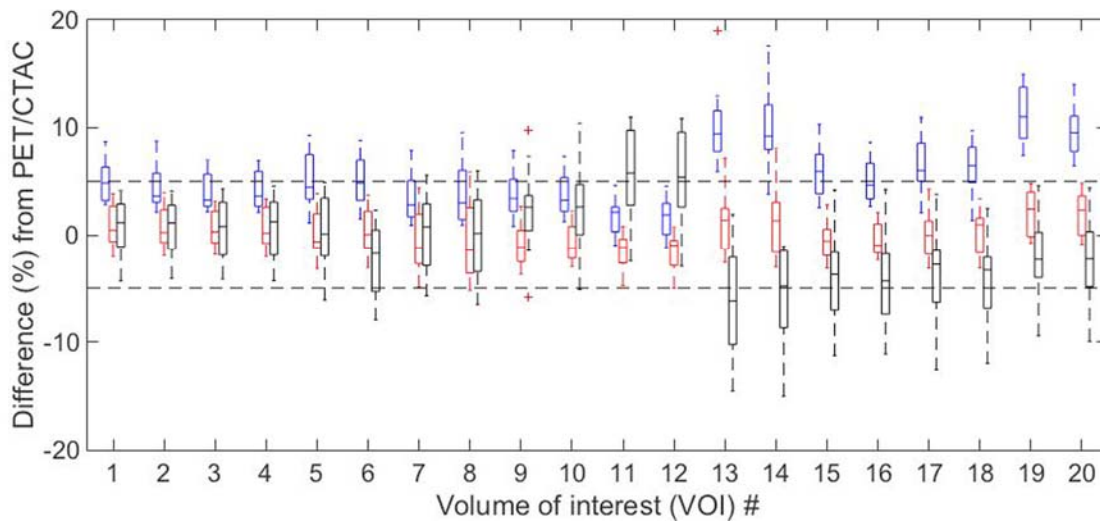
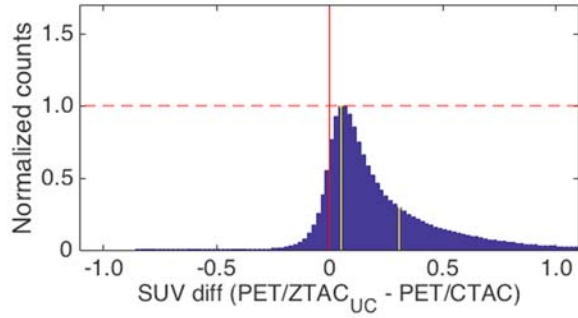
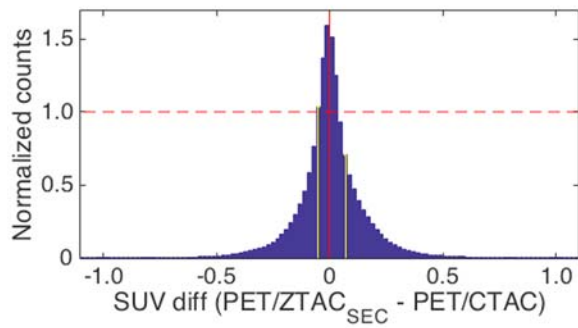


Fig. 4. Box plots of PET uptake differences (%) for 12 patients across 20 VOIs (A) and for 20 VOIs across 12 patients (B) between PET/CTAC and PET/MRAC (left-blue: ZTAC_{UC}, middle-red: ZTAC_{SEC}, right-black: ATAC). The tops and bottoms of each "box" are the 25th and 75th percentiles of the samples, respectively, with the median and an outlier (+ sign, $> 1.5 \times$ interquartile range).

A



B



C

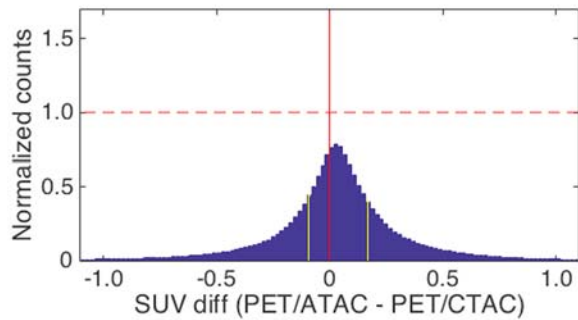


Fig. 5. Histograms of voxel-based PET uptake differences (PET/MRAC - PET/CTAC) across all patients using the voxels within the standardized uptake value (SUV) range of 0.5-15.0 (g/ml). (A) ZTAC_{UC} (B) ZTAC_{SEC} (C) ATAC. Counts were normalized by the maximum count of PET/ZTAC_{SEC} difference from PET/CTAC. Left-right yellow lines indicate the 25th and 75th percentiles.

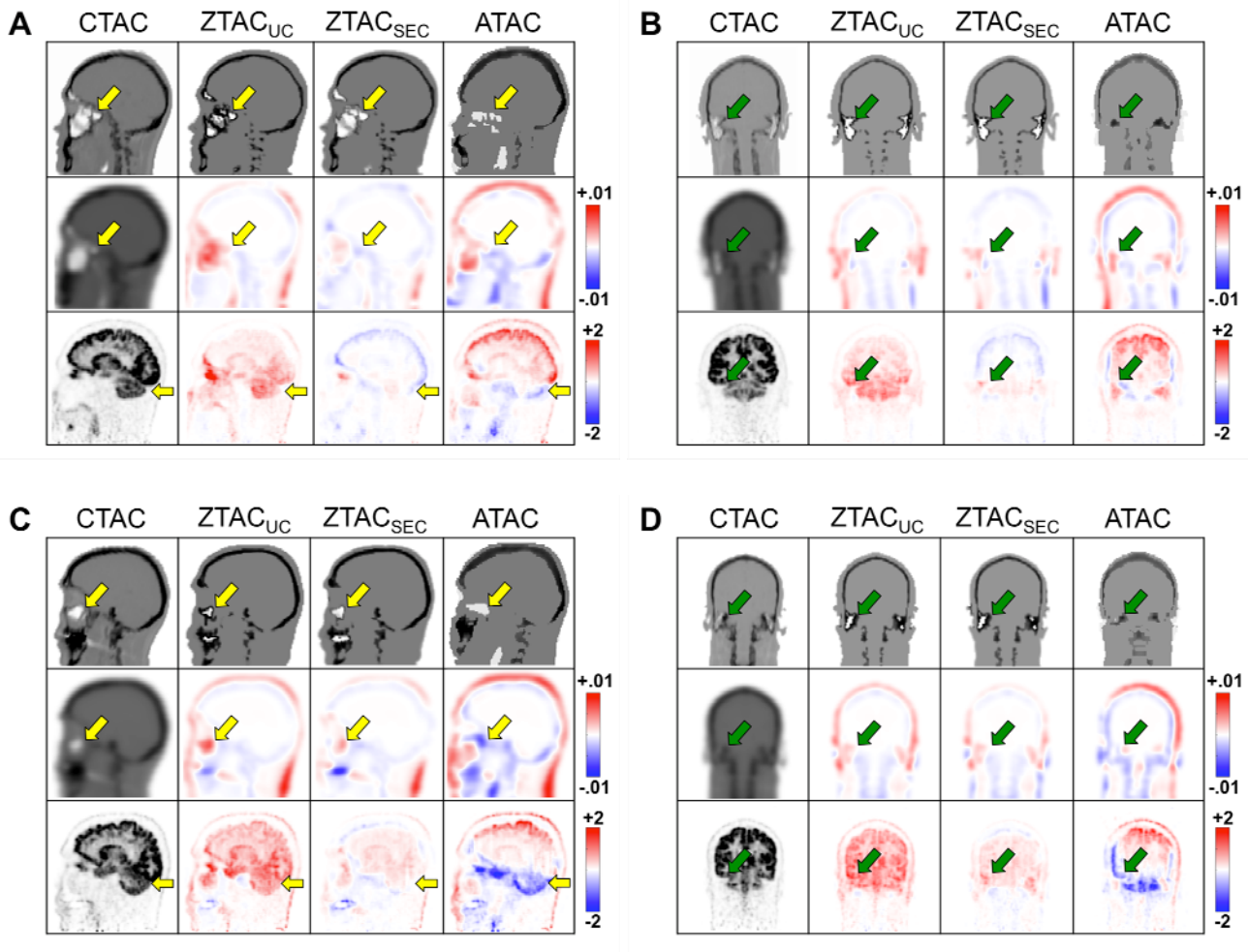


Fig. 6. Patient 5 (A,B) and 8 (C,D) in the coronal and sagittal views for CT and pseudoCTs (1st row), attenuation correction (AC) maps (2nd row), and corresponding PET images (3rd row) according to the AC methods. The 2nd and 3rd rows illustrate the difference images on 2nd – 4th columns for pseudoCT-derived AC maps from CT-derived AC maps (unit: cm^{-1}) and PET/MRAC from PET/CTAC (unit: SUV), respectively. Arrows indicate the sinus, mastoid, and cerebellum regions.